ESTIMATING FIBER ORIENTATION DISTRIBUTION WITH APPLICATION TO STUDY BRAIN LATERALIZATION USING HCP D-MRI DATA

By Seungyong Hwang^a, Thomas C. M. Lee^b, Debashis Paul^c and Jie Peng^d

Department of Statistics, University of California, Davis, ^asyhwang@ucdavis.edu, ^btcmlee@ucdavis.edu, ^cdebpaul@ucdavis.edu, ^djiepeng@ucdavis.edu

Diffusion-weighted magnetic resonance imaging (D-MRI) is an in vivo and noninvasive imaging technology for characterizing tissue microstructure in biological samples. A major application of D-MRI is for white matter fiber tract reconstruction in brains. It begins by estimating the water molecule movements (serving as proxies for fiber directions) in the brain voxels and then combines the results to form fiber tracts. The voxel-level fiber direction information can be modeled by a fiber orientation distribution (FOD) function, and in this paper, we propose a computationally scalable FOD estimator, the blockwise James-Stein (BJS) estimator. We then apply BJS to the D-MRI data from the *Human Connectome Project (HCP)* to study brain lateralization, an important topic in neuroscience. Specifically, we focus on the association between lateralization of the superior longitudinal fasciculus (SLF)—a major association tract and handedness. For each subject from the HCP data, we extract voxel-level directional information by BJS and then reconstruct the SLF in each brain hemisphere through a tractography algorithm. Finally, we derive a lateralization score that quantifies hemispheric asymmetry of the reconstructed SLF. We then relate this lateralization score to gender and handedness through an ANOVA model, where significant handedness effects are found. The results indicate that the SLF lateralization is likely to be different in right-handed and left-handed individuals. Codes and example scripts for both synthetic experiments and HCP data application can be found at https://github.com/vic-dragon/BJS.

1. Introduction. Diffusion-weighted magnetic resonance imaging (D-MRI) is a widely used, noninvasive tool to probe tissue microstructure of biological samples in vivo through measuring water diffusion characteristics. The most important application of D-MRI is the reconstruction of white matter fiber tracts—large axon (a.k.a. nerve fiber) bundles with similar destinations in the brain. By mapping white matter fiber tracts, we can study the structural organization of neuronal networks and understand brain functionality (Mori (2007), Sporns (2011)). For an example of reconstructed white matter fiber tracts, see Figure 10. D-MRI has also been used in other clinical applications, such as detecting brain abnormality in white matter due to axonal loss or deformation, which are related to many neurodegenerative diseases, including Alzheimer's disease, and surgical planning by resolving complex neuronal connections between white and gray matters (Nimsky, Ganslandt and Fahlbusch (2006)).

In the following we first give a brief description of the D-MRI technology and data acquisition. We then introduce our D-MRI data application, followed by the review of two common D-MRI statistical models. Finally, we highlight our contributions.

1.1. Diffusion MRI. MRI technology can measure signals from various nuclei, whereas diffusion MRI focuses on signals from protons. Since in the human body the majority (>90%) of protons are from water molecules, signals from D-MRI experiments of human brains are sensitized to the intensity and direction of water diffusion.

Received April 2022; revised May 2023.

In a D-MRI experiment of the brain, a subject lies in an MRI machine with the head placed inside a strong homogeneous magnetic field (referred to as the b_0 - field). The brain tissue is then excited by applying direction-specific magnetic field gradients (i.e., magnetic fields changing along specific directions) and pulses of radio frequency energy. Measurements are taken on the frequency characteristics of the energy emitted from the excited tissue. These measurements allow us to estimate, at each location in the brain (referred to as a *brain voxel*), the bulk amount of water diffusion occurring along each of the magnetic field *gradient directions* (represented by unit-length vectors in \mathbb{R}^3).

Specifically, at the beginning of the experiment and induced by the b_0 field, water molecules at different locations within a voxel resonate at the same frequency and with the same phase. After turning on a magnetic field gradient for a short period of time (1 \sim 100 ms), water molecules start to resonate at different frequencies, depending on their locations, as different gradient field strengths were experienced at different locations. Consequently, signals will be out of phase (referred to as *dephasing*), and this phase disruption leads to an overall signal loss. The gradient field is then turned off for a short period of time, followed by an identical (in terms of direction and strength) gradient application with the opposite polarity such that the phase disruption will be (partially) recovered (referred to as *rephasing*). Perfect rephasing only happens when water molecules remained stationary between the two gradient applications. On the other hand, if water molecules had a significant movement between these two gradient applications, there would be a disruption of phase across the sample, even after rephasing, which leads to an overall *signal attenuation* (*loss*). This is the reason that D-MRI measurements are also known as *diffusion weighted measurements*.

Suppose at a particular voxel, water mainly diffuses along the left-right direction. Then, for gradient applications perpendicular to the left-right direction (e.g., those along the superior-inferior or anterior-posterior directions), there would be little signal attenuation because there is little water motion along those directions. As a result, at this voxel the signal intensity corresponding to such gradient applications would be (nearly) the same as the baseline signal intensity. On the other hand, if a gradient application is along the left-right direction, then there would be high signal attenuation such that at this voxel, the signal intensity corresponding to the left-right gradient application would be (much) smaller than the baseline signal intensity.

In biological samples containing fatty tissues (such as the brain), water diffuses preferentially along tissue structures (such as white matter fiber tracts). This is referred to as *anisotropic diffusion*. Consequently, D-MRI signals also display strong directional attenuation and thus can be used to probe the anatomy of biological samples.

In addition to the directions of water diffusion and gradient application, the amount of signal attenuation at a voxel is also affected by other factors, including the b_0 -field strength and the duration of gradient applications. The aggregated effect of these factors is reflected by an experimental parameter called the b-value. In short, the higher the b-value, the greater is the amount of signal attenuation and the more sensitive are D-MRI measurements to water diffusion. For more details of the D-MRI technology and data acquisition, the readers are referred to Jones (2010), Le Bihan et al. (2001), Mori (2007).

1.2. HCP D-MRI application. In this work we are interested in investigating brain lateralization (or hemispheric asymmetry), specifically, the association between superior longitudinal fasciculus (SLF) lateralization and handedness, using the Human Connectome Project (HCP) (Essen et al. (2013)) D-MRI data. Brain lateralization refers to the tendency for some neural functions to be specialized to one hemisphere of the brain. Handedness refers to an individual's preference in using one hand over another, which is a key feature of human motor behavior. The asymmetrical functions of the hands are believed to reflect asymmetries in brain function and structure (Budisavljevic, Castiello and Begliomini (2021)).

The most well-known example of brain lateralization is the lateralization of the language pathway, and it has been studied recently through neuroimaging technologies, including D-MRI and functional MRI (fMRI). For example, Catani et al. (2007) and Gharabaghi et al. (2009) investigated the perisylvian language pathway, the direct connections between Broca's and Wernicke's territories, through D-MRI tractography. Houston et al. (2019) investigated the association of diffusion tensor imaging (DTI) metrics with language function and demographic features, including age and gender, by making use of tract based spatial statistics (Smith et al. (2006)). Szaflarski et al. (2012) investigated language lateralization in left-handed children through fMRI. Lateralization of other pathways, such as the motor pathway, has also been studied through imaging technologies. For example, Seizeur et al. (2014) studied the association between corticospinal tract asymmetry and handedness through D-MRI tractography. For a review of recent studies of the relationship between handedness and various white matter tracts of the brain, we refer to Budisavljevic, Castiello and Begliomini (2021).

The main motivation to focus on SLF in this paper is that the SLF is a large lateral association fiber tract, located in each hemisphere, involved in motor, visual, spatial, memory, and language functions (Makris et al. (2004)). There are some recent studies on the relationship between SLF structure and hand motion and handedness. For example, Budisavljevic et al. (2017) explored how selective the three association fronto-parietal branches of the SLF are for different kinds of hand movements through correlating D-MRI tractography results and kinematic data in 30 right-handed subjects. They demonstrated that differences in SLF structure and asymmetry were associated with visuomotor processing. Howells et al. (2018) used tractography results of 51 healthy adults to evaluate differences in the three SLF tracts asymmetry between right-handed and left-handed subjects and its association with manual specialization across a range of motor tasks. Amemiya, Naito and Takemura (2021) studied age dependency and lateralization of SLF tracts using the fractional anisotropy (FA) value and tract volume data derived from coregistered T1 and D-MRI images of 82 predominantly right-handed healthy subjects.

In this paper we leverage the large sample size of the HCP data to investigate the association between SLF lateralization and handedness. Specifically, we select a gender-balanced subset from the HCP young adults data that consists of D-MRI measurements and demographic information of 184 unrelated subjects, including 46 left-handed subjects and 138 right-handed subjects. D-MRI data from HCP have diffusion weighted measurements taken under three different *b*-values (1000 s/mm², 2000 s/mm², 3000 s/mm²). For each *b*-value, at each voxel (size: $1.25 \times 1.25 \times 1.25 \text{mm}^3$) on a $145 \times 174 \times 145$ 3D brain grid, there are measurements corresponding to a common set of 90 distinct gradient directions. Moreover, six nondiffusion weighted images (referred to as b_0 images) are obtained under the constant background magnetic field (b_0 - field). In summary, for each of the three b-values a HCP D-MRI data set consists of 96 grey scale images on a 145 × 174 × 145 3D grid, along with 90 3D unit vectors representing the 90 gradient directions. We first estimate the fiber direction(s) at each voxel, and then we combine such voxel-level directional information for SLF reconstruction through a tractography algorithm. We then derive a lateralization score that quantifies hemispheric asymmetry of the reconstructed SLF. We relate this lateralization score to gender and handedness—two commonly considered demographic/behavioral features in brain lateralization studies—through an ANOVA model. Significant handedness effects were observed, indicating that the SLF lateralization is likely to be different in righthanded and left-handed individuals. In the following we first introduce two commonly used models for extracting voxelwise directional information from D-MRI data.

1.3. Single tensor model. One of the earliest and still widely used D-MRI models for estimating watering diffusion at each voxel is the *single tensor model*, where the diffusion process is modeled by a 3D Gaussian distribution whose covariance matrix is referred to as the *diffusion tensor* (Mori (2007)). The single tensor model is the reason that D-MRI is also called *diffusion tensor imaging (DTI)*.

Specifically, the (noiseless) diffusion weighted signal at voxel \mathbf{v} along a gradient direction \mathbf{x} , expressed as a 3D unit-length vector, is given by

(1)
$$S(\mathbf{v}, \mathbf{x}) = S_0(\mathbf{v}) \exp\{-b\mathbf{x}^{\mathsf{T}} \mathbf{D}(\mathbf{v}) \mathbf{x}\},\$$

where $S_0(\mathbf{v})$ is the nondiffusion-weighted signal intensity at \mathbf{v} , $\mathbf{D}(\mathbf{v})$ is a 3 × 3 positive definite matrix denoting the diffusion tensor at \mathbf{v} , and b > 0 is the *b-value*. As a tensor has only six parameters, the single tensor model can be fitted with as few as seven diffusion measurements.

Notice that if \mathbf{x} is aligned with the principal eigenvector of $\mathbf{D}(\mathbf{v})$, then we will observe the strongest signal attenuation. Once we obtain an estimated diffusion tensor $\hat{\mathbf{D}}(\mathbf{v})$, the voxel-level fiber/diffusion orientation is extracted as the principal eigenvector of $\hat{\mathbf{D}}(\mathbf{v})$ and used as inputs in tractography algorithms for white matter tract reconstruction (Basser et al. (2000)).

The single tensor model also provides some useful image contrasts, most notably, the *fractional anisotropy (FA)* that quantifies the degree of anisotropic diffusion at a voxel,

(2)
$$FA := \sqrt{\frac{1}{2}} \frac{\sqrt{(\lambda_1 - \lambda_2)^2 + (\lambda_2 - \lambda_3)^2 + (\lambda_3 - \lambda_1)^2}}{\sqrt{\lambda_1^2 + \lambda_2^2 + \lambda_3^2}},$$

where $\lambda_1 \geq \lambda_2 \geq \lambda_3 > 0$ are the three eigenvalues of the diffusion tensor $\mathbf{D}(\mathbf{v})$ at that voxel. When the diffusion is isotropic (i.e., $\lambda_1 = \lambda_2 = \lambda_3$), the FA value reaches the lower limit 0, and while the diffusion is highly anisotropic (i.e., $\lambda_1 \gg \lambda_2, \lambda_3$), the FA value approaches the upper limit 1.

1.4. FOD model for crossing fibers. As one may expect, the above single tensor model cannot resolve *intravoxel orientational heterogeneity*, which happens when a voxel has multiple fiber populations with distinct orientations. This is estimated to be present in about 30% white matter voxels, and, therefore, in such regions any single tensor model would lead to misleading FA values and poor direction estimation that adversely affects fiber reconstruction. The SLF in our application is known to be difficult to reconstruct due to the crossings between its fibers and those from the corticospinal tract (CST) (Catani (2010)).

This motivates us to employ a model that expresses the D-MRI signal at each voxel as a convolution of an underlying *fiber orientation distribution (FOD)* function and an axially symmetric response function (Tournier et al. (2004)). See Figure 1 for a graphical illustration at a voxel with two fiber bundles crossing at 60°, and see also (3) in Section 2.1 for a mathematical description of the FOD model. When compared with the single tensor model (1), the FOD model (3) is capable of handling intravoxel heterogeneous fiber populations. Note that,

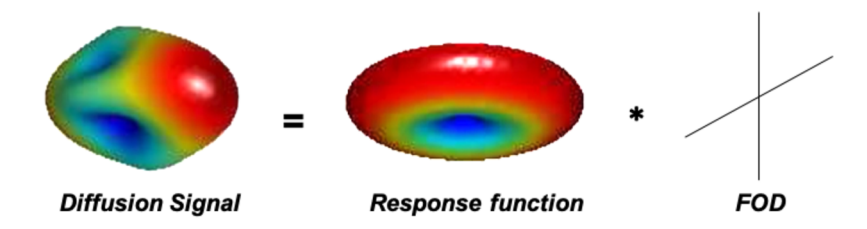


FIG. 1. FOD model of D-MRI signal: At a voxel with two fibers crossing at a 60° separation angle.

when the two smaller eigenvalues of $\mathbf{D}(\mathbf{v})$ are the same, the single tensor model (1) becomes a special case of the FOD model (3) with a single fiber direction.

The FOD model directly describes the local spatial arrangement of axonal fiber bundles and thus is particularly attractive when the downstream goal is white matter fiber tract reconstruction (as in our application). Particularly, the FOD model is able to resolve crossing fibers within a voxel at the expense of requiring *high angular resolution diffusion imaging* (*HARDI*) data (Tuch et al. (2002), Hosey, Williams and Ansorge (2005)), where a large number of gradients (such as in the HCP D-MRI experiments that this paper studies) is sampled.

Since FOD describes the distribution of fiber bundle orientation at each voxel, it is reasonable to think of the FOD as a smooth function with a few sharp peaks, where each peak corresponds to a distinct major fiber bundle within the voxel, or no peak at all in case of isotropic diffusion. Once the FOD is estimated, the peak directions can be extracted and then used as inputs for tractography algorithms. This means that, in the presence of any fiber bundle in the voxel, it is imperative for the estimators to have sufficient *angular resolution*, that is, sharp peak(s).

1.5. *Contributions*. In addition to the successful identification of significant handedness effects in the SLF lateralization that enhances our understanding of brain lateralization and brain function, this paper also makes two other major contributions as described below.

The first one is the development of a *blockwise James–Stein* type estimator, referred to as *BJS*, for FOD estimation at each voxel. Through extensive synthetic experiments, we compare *BJS* with two other FOD estimators, namely, *SHridge* that uses a ridge-type penalty (Descoteaux et al. (2006), Yan et al. (2018)) and *SCSD* that applies an iterative superresolution sharpening (Tournier, Calamante and Connelly (2007)) upon the *SHridge* estimator. The results demonstrate that *BJS* achieves competitive performance in terms of direction estimation, particularly in maintaining angular resolution. It is also at least 10 times faster than the other two methods. The computational efficiency of *BJS* is important for the kind of applications considered in this paper, where the FOD model needs to be fitted on a large number of voxels per image (in our application $\sim 100k$) for a large number of images (here ~ 200).

The other major contribution of this paper is the proposal of a data analysis pipeline that can be used to identify potential associations amongst D-MRI derived brain structural connectivity features and external variables. The pipeline is illustrated in Figure 2 and includes the following major steps:

- 1. *Preprocessing*: Conducting brain extraction, white matter segmentation, and registration using the software *FSL* version 6.0.0 (Jenkinson et al. (2012)) and R packages *fslr* (Muschelli et al. (2015)) and *neurohcp* (Muschelli (2018)) from the *neuroconductor* repository.
- 2. ROI masks: Creating masks for the region of interests (ROIs) using FSLeyes (McCarthy (2020)) and the JHU White-Matter Tractography Atlas (Hua et al. (2008), Wakana et al. (2007)).
- 3. FOD estimation and peak detection: Deriving FOD estimates for the white-matter voxels within the masks and extracting the peaks of the estimated FODs by a peak detection algorithm (Yan et al. (2018)).
- 4. Fiber tracts reconstruction: Using extracted peak directions as inputs in a deterministic tractography algorithm—DiST (Wong et al. (2016)) as well as applying streamline selection to further improve the reconstruction.
 - 5. Feature extraction: Extracting brain connectivity related features.
- 6. *Group analysis*: Relating the extracted features to external variables of interest through appropriate statistical models.

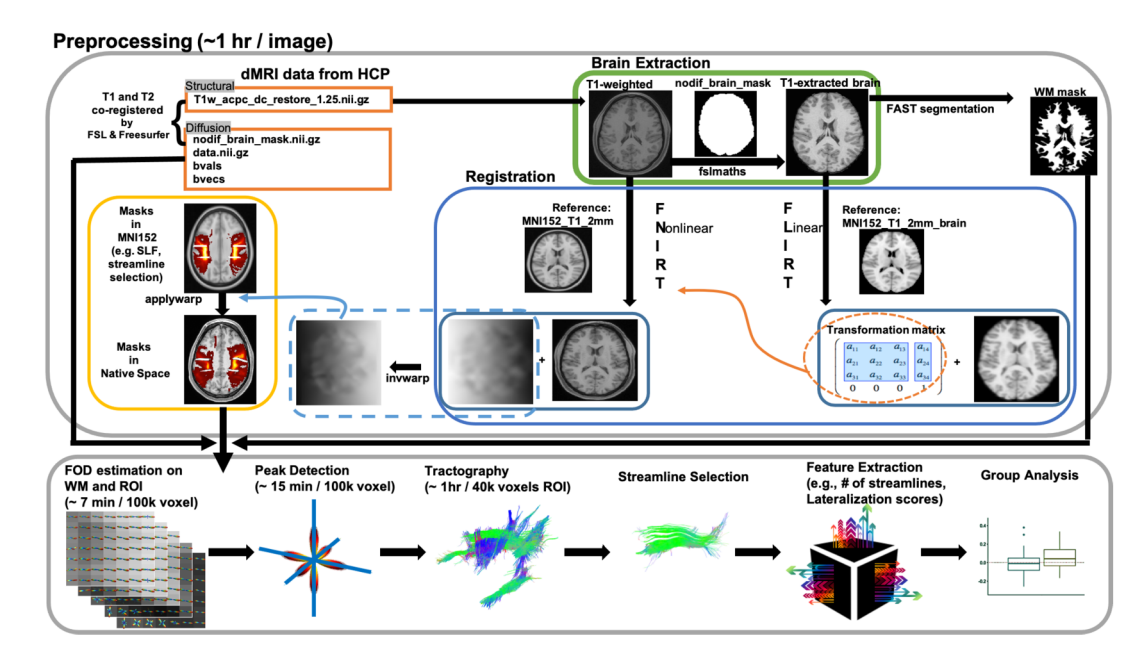


FIG. 2. Schematic plot of data analysis pipeline for D-MRI applications. (Processing time is under a Xeon 72 core, 2.3GHz, 256GB RAM linux server).

The rest of the paper is organized as follows. Section 2 describes the FOD model and the proposed *BJS* estimator. In Section 3 *BJS* is compared with two competing methods through synthetic experiments. Section 4 describes the HCP D-MRI data and reports our application on the SLF lateralization. We conclude the paper with a discussion in Section 5. Further details can be found in the Supplementary Material. (Hwang et al. (2024))

- **2. Methodology.** This section first describes the FOD model, followed by a discussion of two existing FOD estimators, *SHridge* and *SCSD*. We then present the proposed estimator *BJS*, which achieves superior or similar performance as *SHridge* and *SCSD*, albeit being computationally much more efficient. We first note that, in general, a FOD is a probability density function defined on the unit sphere.
- 2.1. FOD model and SH representation. The FOD model assumes that the diffusion signal at each voxel is a spherical convolution between the response function—an axially symmetric convolution kernel that characterizes water diffusion when there is a single dominant fiber bundle aligned with the z-axis (the bottom-top axis)—and the FOD of fiber bundle orientation at that voxel. More precisely, it assumes that the (noiseless) diffusion weighted signal at voxel ${\bf v}$ along a gradient direction ${\bf x}$ is given by

(3)
$$S(\mathbf{v}, \mathbf{x}) = \int_{\mathbb{S}^2} R(\mathbf{x}^T \mathbf{y}) F(\mathbf{v}, \mathbf{y}) d\omega(\mathbf{y}), \quad \mathbf{x} \in \mathbb{S}^2,$$

where $d\omega(\mathbf{y})$ is the volume element of the 3D unit sphere \mathbb{S}^2 , $F(\mathbf{v}, \cdot)$ is a symmetric spherical probability density function, and $R(\cdot)$ is an axially symmetric kernel and is assumed to be the same across voxels and fiber bundles.

In practice, we can reliably estimate $R(\cdot)$ in (3) by using only voxels with a single dominant fiber bundle, for example, those that have a high FA value under the single tensor model (1). In fact, it is shown in Yan et al. (2018) that the FOD model is quite robust to the specification of the response function; see Section 4.3 for details. Therefore, for simplicity, in sequel $R(\cdot)$ is assumed known. Moreover, hereafter, we suppress the dependency on voxel

index v in S and F. Our goal is to estimate the FOD $F(\cdot)$ based on the observed diffusion measurements. As can be seen from model (3), this amounts to a *spherical deconvolution* problem.

Since $S(\cdot)$, $F(\cdot)$, and $R(\cdot)$ are real and symmetric functions, they can be represented by real symmetrized spherical harmonic (SH) basis. Let $\{\widetilde{\Phi}_{lm}: -l \le m \le l; l = 0, 1, \ldots\}$ denote the complex SH basis. Then a real symmetrized SH basis is defined as (Descoteaux et al. (2007)),

(4)
$$\Phi_{lm} = \begin{cases} \sqrt{2} \cdot \Re(\widetilde{\Phi}_{lm}) & \text{if } -l \leq m < 0, \\ \widetilde{\Phi}_{l0} & \text{if } m = 0, \\ \sqrt{2} \cdot \Im(\widetilde{\Phi}_{lm}) & \text{if } 0 < m \leq l, \end{cases}$$

for l = 0, 2, 4, ..., where $\Re(z)$ and $\Im(z)$ denote the real and imaginary parts of $z \in \mathbb{C}$, respectively.

Since the response function $R(\cdot)$ is axially symmetric, $\langle R, \Phi_{lm} \rangle = 0$, unless m = 0. Let $r_l = \langle R, \Phi_{l0} \rangle$ and $f_{lm} = \langle F, \Phi_{lm} \rangle$ be the SH coefficients of $R(\cdot)$ and $F(\cdot)$, respectively. Then, by equation (3) and a standard result of the convolution property of the spherical harmonics (Healy, Hendriks and Kim (1998)), the D-MRI signal $S(\cdot)$ has SH coefficients,

(5)
$$s_{lm} = \langle S, \Phi_{lm} \rangle = \sqrt{\frac{4\pi}{2l+1}} r_l f_{lm}, \quad -l \le m \le l; l = 0, 2, \dots$$

The observed D-MRI measurements $\{y_i\}_{i=1}^n$ are noisy corrupted versions of $S(\cdot)$ measured along n gradient directions $\{\mathbf{x}_i\}_{i=1}^n$. The major source of noise (after removing artifacts due to eddy currents, echo planar imaging distortion and subject motion) in D-MRI data is the thermal noise in the MRI scanner. It is modeled as independent and additive white noise on the real and imaginary parts of the signal. Since the observed D-MRI measurements are ℓ_2 norms of the complex-valued signal from the MRI scanner, they follow a *Rician distribution* (Gudbjartsson and Patz (1995)). However, when the *signal-to-noise ratio* (SNR) level is high, as is the case of HCP D-MRI data (see Figure 7), Rician noise can be approximated by additive Gaussian noise (Carmichael et al. (2013)).

Use \mathbf{I}_{2l+1} and \mathbf{I}_n to denote the $(2l+1)\times(2l+1)$ identity matrix and $n\times n$ identity matrix, respectively. Under the assumption that a finite level (up to l_{\max}) of SH basis can represent $S(\cdot)$ and $F(\cdot)$, the D-MRI measurements can then be modeled as

(6)
$$\mathbf{y} = \mathbf{\Phi} \mathbf{R} \mathbf{f} + \boldsymbol{\varepsilon}, \quad \boldsymbol{\varepsilon} \sim N(0, \sigma_{\varepsilon}^2 \mathbf{I}_n),$$

where **R** is an $L \times L$ diagonal matrix $(L = \frac{(l_{\max}+1)(l_{\max}+2)}{2})$ being the total number of SH basis) with the lth diagonal block equal to $r_l \sqrt{4\pi/(2l+1)} \cdot \mathbf{I}_{2l+1}$, for $l = 0, 2, \dots, l_{\max}$. Also, Φ is the $n \times L$ matrix with the elements in the ith row and (l, m)th column, given by $\Phi_{lm}(\mathbf{x}_i)$, and $\mathbf{f} = (f_{lm})$ is the $L \times 1$ vector of SH coefficients of the FOD $F(\cdot)$. Moreover, the vector $\boldsymbol{\varepsilon} = (\varepsilon_i)_{i=1}^n$ represents observational noise and is assumed to have independent coordinates that follow a Gaussian distribution with $\mathbb{E}(\varepsilon_i) = 0$ and $\mathrm{Var}(\varepsilon_i) = \sigma_{\varepsilon}^2$.

In order to achieve sufficient angular resolution, higher-order spherical harmonics are needed to represent the FOD (i.e., sufficiently large $l_{\rm max}$). In practice, we choose $l_{\rm max}$ to be the largest even number such that the sample size n is still greater than the number of SH basis L. Specifically, in the synthetic experiments $l_{\rm max}=6,10,12$ (L=28,66,91) for n=41,81,321 gradient directions, respectively, and in the HCP application, $l_{\rm max}=10$ (L=66) is used, as there are n=90 gradient directions.

Also, note that, due to the decay of the singular values of the design matrix resulting from the decrease of higher order SH coefficients of the response function $R(\cdot)$, deconvolution becomes increasingly unstable and more susceptible to noise amplification when higher order harmonics are used in FOD representation. Therefore, appropriate regularization is required for accurate FOD estimation and fiber direction extraction.

2.2. SHridge and SCSD. The SHridge estimator is motivated by Descoteaux et al. (2006) who proposed the Laplace–Beltrami regularization to estimate the orientation distribution function (ODF) (Tuch (2002), Tuch (2004)). The same penalty can be used for FOD estimation (Yan et al. (2018)),

(7)
$$\min_{f} \|\mathbf{y} - \mathbf{\Phi} \mathbf{R} \mathbf{f}\|_{2}^{2} + \lambda \mathbb{E}(F), \qquad \mathbb{E}(F) := \int_{\Omega} (\Delta_{b} F)^{2} d\Omega = \mathbf{f}^{T} \mathbf{P} \mathbf{f},$$

where **P** is an $L \times L$ diagonal matrix with the lth diagonal block equal to $l^2(l+1)^2 \cdot \mathbf{I}_{2l+1}$, for $l = 0, 2, \dots, l_{\text{max}}$, Δ_b is the spherical Laplacian operator, and $\mathbb{E}(F)$ is a measure of roughness of spherical functions. With the objective function (7), the estimated coefficients of FOD are

(8)
$$\hat{\mathbf{f}}^{\text{SHridge}} = (\mathbf{R}\mathbf{\Phi}^T \mathbf{\Phi} \mathbf{R} + \lambda \mathbf{P})^{-1} \mathbf{R}\mathbf{\Phi}^T \mathbf{y}.$$

The tuning parameter λ can be chosen by a grid search and the Bayesian information criterion (BIC) (Schwarz (1978)).

The *SHridge* estimator suffers from low angular resolution and is inaccurate when there are crossing fibers with moderate to small crossing angles (see Section 3). One strategy to improve the angular resolution of FOD estimator is through a *sharpening process* that makes the major peak(s) more prominent and at the same time suppresses small peaks, as they are more likely due to noise. A good example of a sharpening procedure is the *superCSD* method of Tournier, Calamante and Connelly (2007), which iteratively suppresses small and negative values and elevates large values through a super-resolution SH representation (with an order $l_{\text{max}}^s \geq l_{\text{max}}$). Details can be found in Section S.1.1 of the Supplementary Material (Hwang et al. (2024)). We refer to the estimator resulting from applying *superCSD* to *SHridge* as *SCSD*. Although *SCSD* is able to improve upon *SHridge* (see Section 3), it does so at the expense of considerable extra computational overhead.

Next, we propose a new estimator *BJS* that is able to achieve a similar angular resolution as *SCSD*, albeit with much less computational cost.

2.3. Blockwise James-Stein shrinkage estimator (BJS). When the sample size n is greater than the number of SH basis L, then: (i) $\mathbf{\Phi}^T \mathbf{\Phi}$ is well conditioned (under some weak assumptions), and (ii) $\mathbf{R} \mathbf{\Phi}^T \mathbf{\Phi} \mathbf{R}$ is nonsingular. However, due to finite sampling, $\mathbf{\Phi}^T \mathbf{\Phi}$ is not an identity matrix. Also, for large L the matrix \mathbf{R} and, consequently, $\mathbf{R} \mathbf{\Phi}^T \mathbf{\Phi} \mathbf{R}$ becomes significantly ill-conditioned, since r_l decreases to zero as l increases. Therefore, a linear estimator of FOD (e.g., SHridge) is likely to be inefficient. This motivates our proposal of a nonlinear shrinkage procedure, BJS. Notice that blockwise nonlinear shrinkage strategies have been applied successfully for adaptive estimation in nonparametric regression (Cai (1999), Cai, Low and Zhao (2009)) and linear inverse problems (Cavalier and Tsybakov (2002), Cavalier and Tsybakov (2001)).

The *BJS* estimator consists of three steps. First, we transform the data **y** into **z**, which we call the *transformed observations*. We then partition **z** into blocks corresponding to the frequency levels of the SH basis and apply a James–Stein type shrinkage estimator within each block. Since the SH transform of the response function is constant within each harmonic frequency level, the covariance matrix of the transformed data is reasonably homogeneous and well conditioned within each block. Moreover, inspired by Laurent and Massart (2000) and Cavalier and Tsybakov (2001), we adopt a more heavily penalized version of the James–Stein shrinkage that accounts for nonisotropic covariance of the observations, thus allowing for heteroscedasticity as well as dependency among the observations. Finally, we employ a postestimation *one-step* super resolution sharpening to enhance the localized peaks of the estimated FOD. Note that as *BJS* does not involve any grid search or iteration, it is computationally much more efficient than *SHridge* and *SCSD* and scales well for processing a large number of diffusion images. The details of these three steps are as follows:

Step 1: Transformation. Multiply $\mathbf{K} = \mathbf{R}^{-1} (\mathbf{\Phi}^T \mathbf{\Phi})^{-1} \mathbf{\Phi}^T$ to both sides of (6) to obtain the transformed observations,

$$\mathbf{z} = \mathbf{K}\mathbf{y} = \mathbf{f} + \mathbf{K}\varepsilon,$$

where

$$Var(\mathbf{z}) = \sigma_{\varepsilon}^{2} \mathbf{K} \mathbf{K}^{T} = \sigma_{\varepsilon}^{2} \mathbf{R}^{-1} (\mathbf{\Phi}^{T} \mathbf{\Phi})^{-1} \mathbf{R}^{-1} := \sigma_{\varepsilon}^{2} \mathbf{V}.$$

Notice that **z** is the ordinary least squares (OLS) solution.

Step 2: Blockwise James-Stein shrinkage. In this step we estimate **f** through a blockwise James-Stein type estimator by applying an adaptive nonlinear shrinkage within each block. Denote the block of **f** and **z** corresponding to the *l*th level SH basis by $\mathbf{f}^{(l)}$ and $\mathbf{z}^{(l)}$, respectively. The *l*th block consists of (2l+1) coordinates of the respective vector for $l=0,2,4,\ldots,l_{\max}$, and totally, there are $1+\frac{l_{\max}}{2}$ blocks. Let $\mathbf{V}^{(l)}$ be the corresponding $(2l+1)\times(2l+1)$ submatrix of \mathbf{V} and $\boldsymbol{\eta}^{(l)}$ be the *l*th block of the transformed noise vector $\boldsymbol{\eta}:=\mathbf{K}\varepsilon$. Note that $\boldsymbol{\eta}^{(l)}$ follows $N(0,\sigma_{\varepsilon}^2\mathbf{V}^{(l)})$. Moreover, $\mathbf{V}^{(l)}$ equals $\frac{2l+1}{4\pi r_l^2}$ multiplied by the corresponding $(2l+1)\times(2l+1)$ submatrix of $(\boldsymbol{\Phi}^T\boldsymbol{\Phi})^{-1}$. This is because, within each block, \mathbf{R} is a scalar multiple of the identity matrix. Consequently, $\mathbf{V}^{(l)}$ is much better conditioned than \mathbf{V} , and this invites the use of blockwise shrinkage, as described next.

For each level l, we have $\mathbf{z}^{(l)} = \mathbf{f}^{(l)} + \boldsymbol{\eta}^{(l)}$. For $l = 0, 2, ..., l_0$ with $l_0 \ge 2$ a prespecified even number, $\hat{\mathbf{f}}^{(l)} := \mathbf{z}^{(l)}$. For $l > l_0$, we adopt a modified version of James–Stein shrinkage, described in (10), which accounts for the nonisotropic covariance of $\boldsymbol{\eta}^{(l)}$,

(10)
$$\hat{\mathbf{f}}^{(l)} = \left(1 - \frac{\hat{\sigma}_{\varepsilon}^{2}(\|\mathbf{\lambda}_{l}\|_{1} + 2\|\mathbf{\lambda}_{l}\|_{2}\sqrt{t^{(l)}} + 2\|\mathbf{\lambda}_{l}\|_{\infty}t^{(l)})}{\|\mathbf{z}^{(l)}\|_{2}^{2}}\right)_{+} \mathbf{z}^{(l)}, l > l_{0},$$

where λ_l is the vector of eigenvalues of $\mathbf{V}^{(l)}$, $\|\lambda_l\|_1$, $\|\lambda_l\|_2$, $\|\lambda_l\|_\infty$ are ℓ_1 , ℓ_2 , ℓ_∞ norm of λ_l , respectively, $\|\mathbf{z}^{(l)}\|_2^2$ is the squared ℓ_2 norm of $\mathbf{z}^{(l)}$, and $t^{(l)} = c \log(2l+1)$ (c > 1 being a constant) is a regularization parameter. Moreover, $\hat{\sigma}_{\varepsilon}^2$ is the mean squared error (MSE) of the OLS estimates, which is used as an estimator for the error variance σ_{ε}^2 ,

$$\hat{\sigma}_{\varepsilon}^{2} = \frac{\|\mathbf{y} - \mathbf{\Phi}(\mathbf{\Phi}^{T}\mathbf{\Phi})^{-1}\mathbf{\Phi}\mathbf{y}\|}{n - \operatorname{rank}(\mathbf{\Phi})},$$

where $rank(\Phi)$ is the rank of the matrix Φ . Note that, even with an ill-conditioned system, one can still achieve a good fit of the observations by OLS and, consequently, a good estimate of the error variance.

Also, note that shrinkage is only applied to those SH coefficients with a level higher than l_0 , whereas those low order SH coefficients are estimated by OLS. The reason is to avoid excessive bias as low order SH coefficients are expected to be large. Specifically, l_0 should be an even number no less than 2, which limits the possible choices for l_0 . In this paper we set $l_0 = 4$, meaning that we do not shrink the first three levels (i.e., l = 0, 2, 4) of the SH coefficient estimates.

The specific form of the estimator in (10) is motivated by a tail-probability bound for quadratic forms of Gaussian vectors from Laurent and Massart (2000).

Let (w_1, \ldots, w_{2l+1}) be i.i.d. standard Normal random variables and $\lambda = (\lambda_1, \ldots, \lambda_{2l+1})$ be nonnegative constants. Then, the following inequality holds for any t > 0:

$$P\left(\sum_{i=1}^{2l+1} \lambda_i w_i^2 \ge \|\boldsymbol{\lambda}\|_1 + 2\|\boldsymbol{\lambda}\|_2 \sqrt{t} + 2\|\boldsymbol{\lambda}\|_{\infty} t\right) \le \exp(-t).$$

Note that, in the above, the ℓ_1 term $\|\lambda\|_1 = \sum_{i=1}^{2l+1} \lambda_i$ (as λ_i s are nonnegative) is the mean of the random variable $\sum_{i=1}^{2l+1} \lambda_i w_i^2$. And the above inequality is a probabilistic bound on the fluctuation of this random variable above its mean value. The proof by Laurent and Massart (2000) makes usage of the Laplace transform, which gives rise to the ℓ_2 term $\|\lambda\|_{\infty}$.

If, for the lth block, $\mathbf{f}^{(l)} = 0$, then $\mathbf{z}^{(l)} = (\mathbf{K}\varepsilon)^{(l)}$ and follows the distribution of $\sigma_{\varepsilon}^2 \sum_{i=1}^{2l+1} \lambda_{l,i} w_i^2$. By the above tail probability bound, we have $P(\hat{\mathbf{f}}^{(l)} \neq \mathbf{0}) \leq \exp(-t^{(l)}) = (2l+1)^{-c}$, if the regularization parameter $t^{(l)}$ takes the form $c \log(2l+1)$ (with c > 1). Consequently, the probability of falsely detecting a (nonexistent) signal goes to zero. In addition, by the Borel-Cantelli lemma, if there is no signal at all (i.e., all $\mathbf{f}^{(l)} \equiv \mathbf{0}$), then with probability tending to 1 (as $l \to \infty$), except for at most a finite number of blocks, all $\hat{\mathbf{f}}^{(l)}$ will be shrunk to zero. Particularly, for blocks corresponding to higher SH levels, larger shrinkage is applied so that the noise is more aggressively suppressed. In this paper we set c = 2. Based on the results of a sensitivity experiment (Table S.4 in Hwang et al. (2024)), BJS is quite robust with respect to the choice of c.

Step 3: Postestimation sharpening. The evaluation of the estimated FOD on any arbitrary grid is given by $\hat{F} = \tilde{\Phi} \hat{f}$, where $\tilde{\Phi}$ is an $\tilde{n} \times L$ matrix representing the evaluation of the L SH basis on this grid. Since the estimated FOD \hat{F} may have negative values caused by artificial oscillations, to impose nonnegativity the SH coefficients \hat{f} is further updated through a one-step super-resolution sharpening process, using an $l_{\max}^s(\geq l_{\max})$ order SH representation, which not only suppresses negative values but also sharpens the peak(s). In this paper $l_{\max}^s = 16$ is used for the synthetic experiments with separation angle 30°, while for all other cases and the HCP application, $l_{\max}^s = 12$ is used; see Table S.5 in Hwang et al. (2024) for a sensitivity experiment on the effect of l_{\max}^s . Details of the one-step sharpening are available in the Supplementary Material (Section S.1.2 in Hwang et al. (2024)).

Note that both *BJS* and *SCSD* use a nonlinear super-resolution sharpening process. However, there are two major differences. First, *BJS* uses super-resolution sharpening only once, whereas *SCSD* uses a computationally expensive iterative procedure. Second, in *BJS* only negative values are suppressed, while in *SCSD* both negative and small positive values are suppressed. Suppressing small positive values helps the iterative *SCSD* to converge, but it is not required by the one-step *BJS*. In a sensitivity experiment, we examine the effect of suppressing small positive values in the one-step sharpening of *BJS* and find that it does not lead to better estimation (see Table S.6 in Hwang et al. (2024)).

A good initial estimator is crucial for the success of the one-step sharpening process. This is evidenced by the comparison between *BJS* and *SCSD* (Section 3), where *BJS* is able to achieve comparable or better accuracy in FOD estimation, largely due to its superior initial estimator to *SHridge* (which is used as the initial estimator in *SCSD*).

More remarks on the shrinkage factor. Our formulation of the blockwise shrinkage factor in (10) explicitly accounts for heteroscedastic and correlated noise within each block through the eigenvalues of the covariance matrix $\mathbf{V}^{(l)}$ of the lth block. In particular, one important difference of the current setting from those in the existing works is that the covariance matrix of the transformed data is nondiagonal. This is because, due to finite sampling, the design matrix does not diagonalize in the same SH basis as the convolution kernel. Addressing this point requires a careful calibration of the shrinkage factor in BJS.

Cavalier and Tsybakov (2002) solved a linear inverse problem under a Gaussian sequence model with i.i.d. noise, using a blockwise James–Stein shrinkage rule. They first converted the inverse problem to a direct estimation problem with independent but heteroscedastic

noise. They showed that a larger value of the blockwise shrinkage factor than in the ordinary James–Stein shrinkage procedure gave better control on the variance of the estimator at the expense of slightly increased bias. In our context we also deal with an inverse problem, so a good balance between variance and bias of the estimator within each block, which is dictated by the shrinkage factor, is of great importance.

In a closely related setting, though concerning a direct rather than an inverse regression problem involving orthogonal regressors and correlated Gaussian noise, Goldenshluger and Tsybakov (2001) showed that the standard James–Stein estimator still has theoretically near-optimal risk performance (in comparison with the linear oracle estimator) as long as the correlation is mild. In our context empirical analyses show that, for the sampling design we consider, each block of the noise covariance matrix \mathbf{V} is quite well conditioned, even for higher SH level l (condition number is close to 1 for l=4 and less than 1.2 for l=10), while the maximum absolute correlation among the coefficients within each block is modest (around 0.3). Thus, our choice of the shrinkage factor can be seen as a hybrid addressing the combined scenarios dealt with by Cavalier and Tsybakov (2002) and Goldenshluger and Tsybakov (2001). This explains the satisfactory empirical behavior of our proposed BJS.

3. Synthetic experiments. In this section we first compare the running times of the three FOD estimators, namely, *BJS*, *SHridge*, and *SCSD*. Then their performances are assessed through extensive synthetic experiments under different settings in terms of the number of fibers, separation angles between pairs of fiber bundles, the number of gradient directions, *b*-value, and signal-to-noise ratio (SNR).

In the synthetic experiments, the diffusion weighted signals along n gradient directions are generated by adding independent Rician noises to the noiseless diffusion signals. We denote the standard deviation of the real/imaginary components associated with the Rician noise as σ . The noiseless diffusion signals are generated according to the convolution model (3), where the true FOD is set as

$$F(\theta, \phi) = \sum_{k=1}^{K} w_k \delta_{\theta_k, \phi_k}(\theta, \phi), \quad \theta \in [0, \pi], \phi \in [0, 2\pi),$$

with K denoting the number of fiber bundles, $w_k > 0$, $\sum_{k=1}^K w_k = 1$ being the volume fractions, and $\delta_{\theta_k,\phi_k}(.,.)$ being the Dirac delta function at the spherical coordinates (θ_k,ϕ_k) of the kth fiber bundle orientation $(k=1,\ldots,K)$. The volume fractions are set as $w_1=1$ for the K=1 "single-fiber" case; $w_1=w_2=0.5$ for the K=2 "two-crossing fibers" case, and $w_1=w_2=0.3$, $w_3=0.4$ for the K=3 "three-crossing fibers" case. The response function is set as

$$R(\cos(\theta)) = S_0 \exp^{-b(\bar{\lambda}\cos^2\theta + \underline{\lambda}\sin^2\theta)}, \quad \theta \in [0, \pi],$$

where $S_0 = 1$, $\bar{\lambda} = 1 \times 10^{-3} \text{mm}^2/s$, $\underline{\lambda} = 1 \times 10^{-4} \text{mm}^2/s$. Lastly, SNR := S_0/σ .

3.1. Running time comparison. Here we consider the K=1 "single fiber" case with n=81 gradient directions, b-value = 3000 s/mm², and SNR = 50.

The execution times of the three methods across 30 simulation replicates are shown in Figure 3. For *SHridge* a grid with 100 values is used for tuning parameter selection (with BIC). For *SCSD* the additional time by conducting the *superCSD* procedure is reported. Moreover, $l_{\text{max}} = l_{\text{max}}^s = 10$ are used for FOD representation and sharpening, respectively. On average, it took *BJS* 7.246 minutes to process 100k voxels in serial computing on a server with Xeon 72 core processor, 2.3GHz, 256GB RAM. Moreover, Figure 3 shows that *BJS* is at least 10 times faster than the other two methods in terms of both serial and parallel computing.

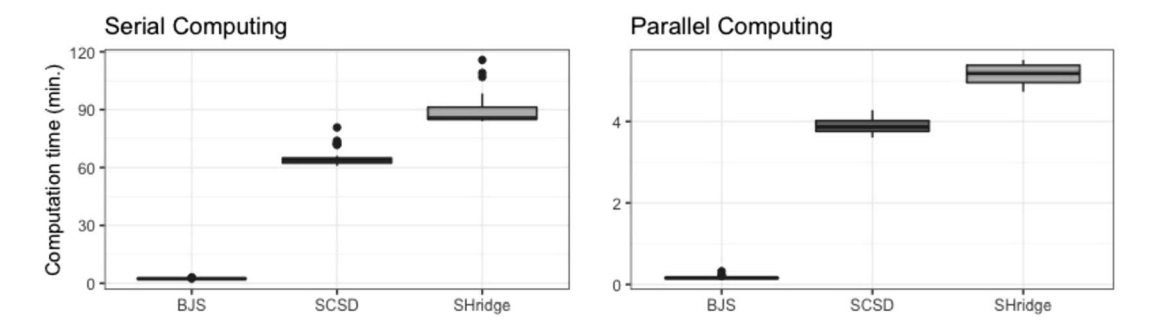


FIG. 3. Execution times: Box plots across 30 replicates; applied to 100k voxels with a single fiber, n = 81, b-value = 3000 s/mm², SNR = 50; set $l_{\text{max}} = l_{\text{max}}^{s} = 10$; evaluated on a server with Xeon 72 core processor, 2.3GHz, 256GB RAM. Left panel—serial computing. Right panel—parallel computing with 30 cores.

3.2. Experimental settings. Here we consider two fibers crossing at five different separation angles (30°, 45°, 60°, 75°, 90°) and three fibers crossing at two different pairwise separation angles (60°, 90°). Also, two different b-values (1000 s/mm², 3000 s/mm²) and two different levels of SNR (20, 50), are considered. Moreover, diffusion signals are sampled along, n = 41, 81, 321, respectively, gradient directions pointing to the centers of the upper-half triangles of an icosphere mesh with increasing orders. For each setting 100 independent replicates of diffusion weighted measurements are generated.

The synthetic experiments cover settings commonly encountered in both clinical and research purpose D-MRI experiments. Especially in the HCP application, we have 90 gradient directions at *b*-value 3000 s/mm² and a median SNR around 50 (Figure 7).

3.3. Evaluation metrics. Estimated FODs are visualized and compared with the true fiber directions in Figure 4, Figures S.1, S.2, and S.3 in Hwang et al. (2024), where the opaque color represents the mean of the estimated FOD (across 100 replicates), the semitranslucent color represents the mean plus two standard deviations of the estimated FODs, and the solid lines represent the true fiber directions.

In many D-MRI applications, including the one studied in this paper, the purpose of FOD estimation is to obtain fiber direction estimates at each voxel, which are then used as inputs in tractography algorithms for white-matter fiber tracts reconstruction. In this paper we use a

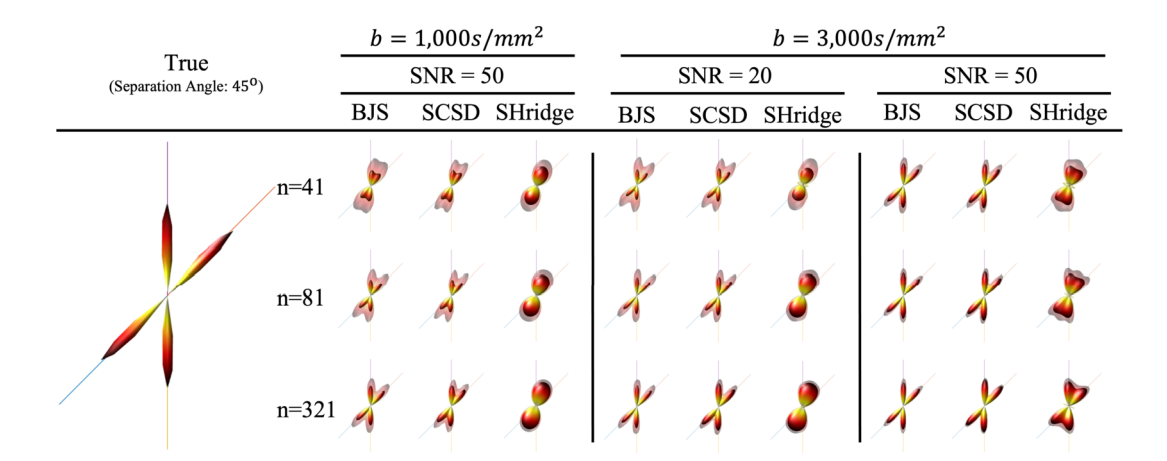


FIG. 4. Synthetic experiment: Two fibers crossing at 45°. The solid lines are the true fiber directions. The opaque part and the semitranslucent part represent, respectively, the mean estimated FODs across 100 replicates and the mean plus two standard deviations of the estimated FODs.

peak detection algorithm (Yan et al. (2018)) to extract the peak(s) of the estimated FOD and use the peak direction(s) as the estimated fiber direction(s). The performance in terms of fiber direction estimation is evaluated by three metrics:

- 1. *D.R.*—Correct peak detection rate, defined as the percentage of replicates where the peak detection algorithm finds the correct number of fibers.
- 2. Bias.Sep—Bias in separation angle estimation, defined as the difference between Mean.Sep and a true separation angle, where the true separation angle is the acute angle between two true directions and Mean.Sep is the acute angle between the two correspondingly estimated fiber directions, averaged across those replicates in which the correct number of fibers is detected, and
- 3. F.D.E.—Fiber direction estimation error, defined as $(1 \cos(\text{angular-error})) \times 10^3$, where angular-error is the acute angle between a true direction and its estimated direction.

These metrics are reported in Table 1, Tables S.1, S.2, and S.3 in Hwang et al. (2024).

3.4. Results. In the case of two fibers crossing at a 45° separation angle (Figure 4 and Table 1), visually, BJS is the best estimator among the three, as, on average, it shows the most accurate direction and retains the angular resolution the best. SHridge performs the worst and shows very poor performance, except for $b = 3000 \text{ s/mm}^2$, SNR = 50 and n = 321. Under $b = 1000 \text{ s/mm}^2$, SCSD performs the best in terms of peak detection rate, whereas under $b = 3000 \text{ s/mm}^2$, both BJS and SCSD can successfully identify two fibers with high rates. In terms of direction estimation (F.D.E.), BJS and SCSD have similar performances, and both are much better than SHridge. However, BJS has considerably less bias in separation angle estimation (Bias.Sep) than SCSD. This phenomenon is observed across nearly all simulation settings considered in this section.

In the case of two fibers crossing at 30° and b-value 3000 s/mm^2 , BJS outperforms both SCSD and SHridge (Figure S.1 and Table S.1 in Hwang et al. (2024)). In terms of peak detection rate, BJS is almost twice as good as SCSD and is much better than SHridge. Moreover, BJS has little bias in separation angle estimation, whereas SCSD tends to severely underestimate the separation angle (thus losing angular resolution) under the high SNR (i.e., 50) settings.

In the case of two fibers crossing at moderate to large separation angles $(60^{\circ}, 75^{\circ}, 90^{\circ})$ (Figure S.2 and Table S.2 in Hwang et al. (2024)) and three fibers crossing at a pairwise separation angle 60° or 90° (Figure S.3 and Table S.3 in Hwang et al. (2024)), *BJS* outperforms *SCSD* in the two-fiber cases and has comparable performance with *SCSD* in the three-fiber cases. Both perform better than *SHridge*.

In summary, when the separation angle is small (i.e., the most challenging settings), *BJS* has a distinct advantage over *SCSD* and *SHridge*. Overall, *BJS* performs the best in separation angle estimation and shows competitive performance in peak detection and fiber direction estimation.

Finally, to assess the impact of FOD estimation on tracking results, we considered a two-dimensional region on a 15×15 voxel-grid with two fiber bundles crossing. We applied these three methods for FOD estimation, extracted the peak directions and then conducted fiber tracking (Wong et al. (2016)). The results are shown in Figure S.4 of the Supplementary Material (Hwang et al. (2024)). It can be seen that BJS and SCSD have similar performance, and both lead to visually more accurate reconstruction than SHridge at the cross region (e.g., for the region indicated by the black box, part of the SHridge reconstruction of the light-gray fiber bundle curved downward instead of following through to the upper-right corner).

As a side note and by the request of a reviewer, we also apply these three methods to a predominantly CSF region of a HCP subject where no dominant fiber direction is expected

TABLE 1
Synthetic experiment: Two fibers crossing at 45°. D.R.: Correct peak detection rate; Bias.Sep: Bias (in arc degree) of separation angle estimation; F.D.E. 1/F.D.E. 2: Fiber direction estimation errors for directions 1 and 2, respectively

		BJS		SCSD			SHridge						
Setting	Design	D.R.	Bias.Sep	F.D.E. 1	F.D.E. 2	D.R.	Bias.Sep	F.D.E. 1	F.D.E. 2	D.R.	Bias.Sep	F.D.E. 1	F.D.E. 2
$b = 1000 \text{ s/mm}^2$, $l_{\text{max}}^s = 12$, SNR = 50	$n = 41, l_{\text{max}} = 6$	62%	-1.33	9.13	8.93	82%	-4.9	7.77	8	3%	29.37	298.23	374.3
	$n = 81, l_{\text{max}} = 10$	83%	-0.59	8.78	7.62	97%	-4.6	7	6.68	0%	-	-	-
	$n = 321, l_{\text{max}} = 12$	100%	-0.16	2.84	2.84	100%	-4.87	2.91	2.6	0%	-	-	-
$b = 3000 \text{ s/mm}^2$, $l_{\text{max}}^s = 12$, SNR = 20	$n = 41, l_{\text{max}} = 6$	92%	-1.71	10.41	9.31	88%	-3.39	3.97	6.64	2%	21.65	460.54	57.61
	$n = 81, l_{\text{max}} = 10$	97%	-1.67	4.71	4.58	98%	-2.59	4.06	2.91	0%	-	-	-
	$n = 321, l_{\text{max}} = 12$	100%	-1.99	2.21	2.75	100%	-1.61	1.25	0.97	1%	-2.08	1.7	2.91
$b = 3000 \text{ s/mm}^2$, $l_{\text{max}}^s = 12$, SNR = 50	$n = 41, l_{\text{max}} = 6$	100%	-1.03	2.06	1.91	100%	-4.55	2.69	1.56	27%	6.28	9.17	4.38
	$n = 81, l_{\text{max}} = 10$	98%	-0.05	0.81	0.73	100%	-2.77	1.35	0.97	33%	0.24	3.79	4.45
	$n = 321, l_{\text{max}} = 12$	100%	-0.34	0.69	0.09	100%	-0.77	0.88	0.09	99%	2.42	1.49	1.5

in most of the voxels. As we can see from Figure S.5 in Hwang et al. (2024), both *BJS* and *SCSD* lead to somewhat noisy estimation in the CSF region, whereas both work relatively well in the nearby white-matter region.

4. HCP D-MRI application. In this section we investigate the association of the SLF lateralization with gender and handedness using data collected from the WU-Minn Human Connectome Project (HCP) (Essen et al. (2013)).

This data set contains Eddy-current-corrected 3T D-MRI data of 1206 healthy young adults (age: 22 to 35) from 457 unique families. D-MRI measurements are taken at three different b-values (1000 s/mm², 2000 s/mm², 3000 s/mm²) on a 145 × 174 × 145 grid with voxel size $1.25 \times 1.25 \times 1.25$

Using the *Edinburgh Handedness Index (EHI)*, we classify the subjects to be left-handed (EHI: -100 to -55) and right-handed (EHI: 85 to 100). Notice that the variability of EHI scores for the left-handed subjects is larger than that for the right-handed subjects. This is probably due to the fact that many left-handed individuals often have some level of mixed dominance, as their surrounding environments tend to be developed for right-handed individuals (López-Vicente et al. (2021)).

In order to remove family effects, we choose at most one subject from each family. If all subjects from a family are right-handed, then a subject is randomly selected. Otherwise, priority is given to left-handed members. We also balance the sample in terms of gender by stratified sampling according to the EHI. Through the above sampling scheme, 184 subjects (left-handed female: 23; left-handed male: 23; right-handed female: 69; right-handed male: 69) are selected. The EHI distribution of these 184 subjects by the gender-handedness group is shown in Figure 5.

Recall that our data analysis pipeline is shown in Figure 2, and the details are given below.

4.1. *Preprocessing*. The D-MRI data are downloaded from the HCP database, *ConnectomeDB*. We note that two images, named T1w and T2w, are accompanied in the data. These T1w and T2w images are typically used for brain extraction and segmentation, respectively. We shall use them in the additional processing steps described below.

In addition, the data have gone through basic quality control and have also been minimally preprocessed Glasser et al. (2013). These steps include: (i) intensity normalization, (ii) EPI distortion correction, (iii) eddy current correction, (iv) gradient nonlinearity correction, and (v) registration of the mean b_0 image (T2w image) to the native volume T1w image and the transformation of diffusion data, gradient deviation, and the gradient directions to the *structural space (T1w space)*. So the HCP D-MRI data have already been *coregistered* to the structural space.

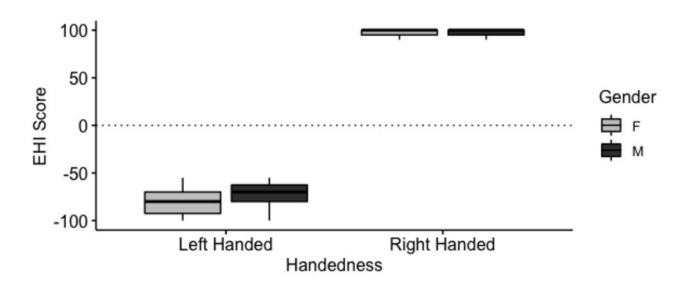


FIG. 5. EHI distribution: Box plots by gender-handedness group of the 184 sampled HCP subjects.

We perform additional processing on each D-MRI image using the software *FSL* version 6.0.0 (Jenkinson et al. (2012)) and R packages *fslr* (Muschelli et al. (2015)) and *neurohcp* (Muschelli (2018)) from the *neuroconductor* repository. The original T1w image contains both skull and the brain. Since the HCP D-MRI data have already been coregistered to the structural (T1w) space, we apply the T2w extracted binary brain mask, provided by HCP, onto the original T1w image to obtain the T1w extracted brain image. Using the T1w extracted brain image and the *FAST* segmentation algorithm (Zhang, Brady and Smith (2001)) in *FSL*, each voxel in the brain is classified into three different tissue types (CSF—cerebrospinal fluid, GM—grey matter, WM—white matter). The segmentation result is used to create a *white-matter mask*. Hereafter, we refer to voxels within the white-matter mask as the *white-matter voxels*. Moreover, the T1w image is registered to a standard space—*MNI152_T1_2mm* (http://www.bic.mni.mcgill.ca/ServicesAtlases/HomePage)—by the *FSL* registration tools FLIRT (Jenkinson et al. (2002)) (for initial linear registration) and FNIRT (Woolrich et al. (2009)) (for subsequent nonlinear registration).

4.2. *SLF masks*. For *superior longitudinal fasciculus (SLF)* reconstruction, we adopt a regional-seeding tractography strategy; see Section 4.4 for details. For this purpose we need to create region of interest (ROI) masks that contain the SLF.

On the MNI152_T1 template space, we use *FSLeyes* (McCarthy (2020)) and the *JHU White-Matter Tractography Atlas* (Hua et al. (2008), Wakana et al. (2007)) to create the SLF masks in the left and right hemispheres, respectively. The left-SLF ROI contains 41,694 voxels, and the right-SLF ROI contains 38,386 voxels. Since it is known that the SLF and the corticospinal tract (CST) are crossing, we further use binary masks from *AutoPtx* (de Groot et al. (2013)) for streamline selection to dissect the SLF from the initial tractography results. As can be seen in Figure 6, the binary masks are situated at the margins of the portions of the SLF masks where the probability of being on the SLF is high, indicated by bright color.

Since all subsequent analyses are conducted on the subject native space, we use the inverse transformation (derived from the registration step) to move the masks on the template space back to the subject native space. On the subject native space, the numbers of voxels in left SLF and right SLF ROIs are $47,379 \pm 5912$ and $42,772 \pm 5430$, respectively. More details on preprocessing and ROI mask creation can be found on https://github.com/vic-dragon/BJS.

4.3. FOD estimation and peak detection. For each subject we first use the white-matter voxels to estimate the response function $R(\cdot)$ in the FOD model (3), following the steps described in Yan et al. (2018). Specifically, at each white-matter voxel we fit the single tensor model (1) and identify voxels with a FA value (2) greater than 0.8 and a ratio between the two

Superior Longitudinal Fasciculus (MNI X=-38, Z=30)

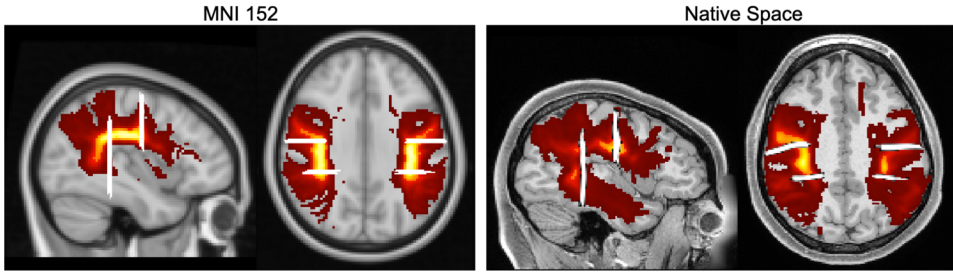


FIG. 6. Left panel—SLF masks on template space (left), right panel—SLF masks on the native space of one HCP subject: The (probabilistic) ROI masks are shown by the heatmap, where brighter color corresponds to a higher probability. The (binary) streamline selection masks are shown by the white strips.

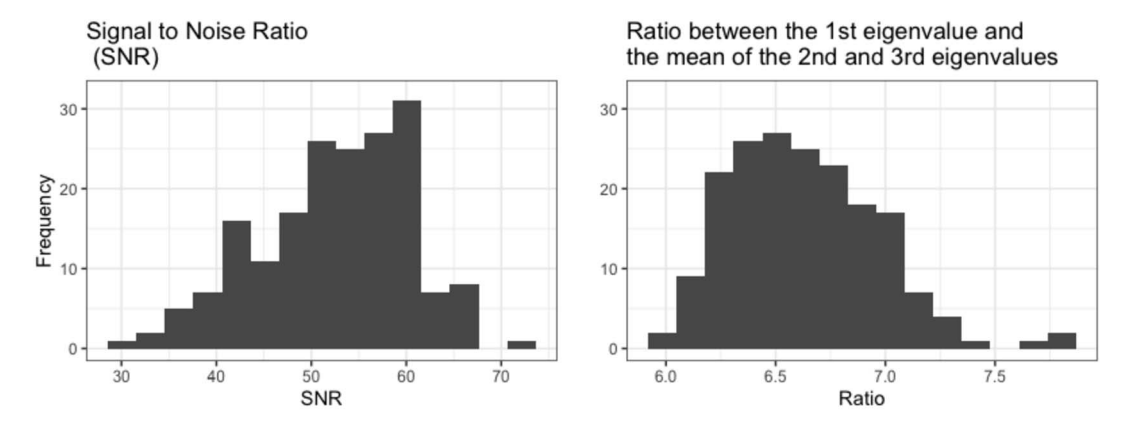


FIG. 7. Histograms of the (estimated) signal-to-noise ratio (left panel) and the ratio between leading and minor eigenvalues of the response function (right panel): Across 184 sampled HCP subjects.

smaller eigenvalues less than 1.5 as having a single dominant fiber bundle. We then calculate the median of the leading eigenvalue and the minor eigenvalue (defined as the average of the two smaller eigenvalues), respectively, across these voxels and denote them by $\bar{\lambda}$ and $\underline{\lambda}$. Then the response function is specified as the diffusion signal along directions in the y-z plane under a single tensor model with $\mathbf{D} = \text{diag}\{\underline{\lambda}, \underline{\lambda}, \bar{\lambda}\}$,

$$R(\cos(\theta)) := S_0 \exp^{-b(\bar{\lambda}\cos^2\theta + \underline{\lambda}\sin^2\theta)}, \quad \theta \in [0, \pi].$$

Note that, in our implementation, we first normalize the DWI measurements at each voxel by the mean intensity of the six b_0 images at that voxel. We then set $S_0 = 1$ in the response function. Since S_0 corresponds to a multiplicative factor in the response function's SH coefficients matrix **R**, such a normalization would not affect the fitted FOD.

For each subject, we also estimate the signal-to-noise-ratio (SNR: = S_0/σ) using the six b_0 images: the overall SNR is taken as the median SNR over all voxels. The estimated SNR and the ratio of the leading and minor eigenvalues of the response function across the 184 selected HCP subjects are shown in Figure 7.

BJS estimates are then obtained for white-matter voxels within the SLF masks. The peak directions of the estimated FODs are extracted by a peak detection algorithm (Yan et al. (2018)). Moreover, nonwhite-matter voxels within the SLF masks are automatically specified as isotropic and thus have no associated peak direction. The peak detection algorithm associates each voxel with either none, one, or multiple directions, and they are used as inputs in the deterministic tracking algorithm DiST (Wong et al. (2016)) for the SLF reconstruction described in Section 4.4.

4.4. SLF reconstruction by tractography and streamline selection. In neuroscience tractography refers to the technique of reconstructing and visually representing white-matter fibers using D-MRI data. While applying a tractography algorithm, there are several options for seeding and terminating criteria. Tracking is initialized at so-called seed locations, and there are generally two options: whole-brain seeding vs. seeding within a ROI, referred to as regional-seeding. For terminating criteria, common choices include trajectory bending more than a prespecified angle in a single step, trajectory entering a region of low FA, or trajectory leaving the white-matter segment. Moreover, tracking may be terminated when the trajectory leaves the ROI. For an overview of deterministic tractography, see Alexander (2010).

Here we apply the *DiST* tracking algorithm (https://github.com/vic-dragon/dmri.tracking), a deterministic tractography algorithm that can handle zero or multiple directions within one

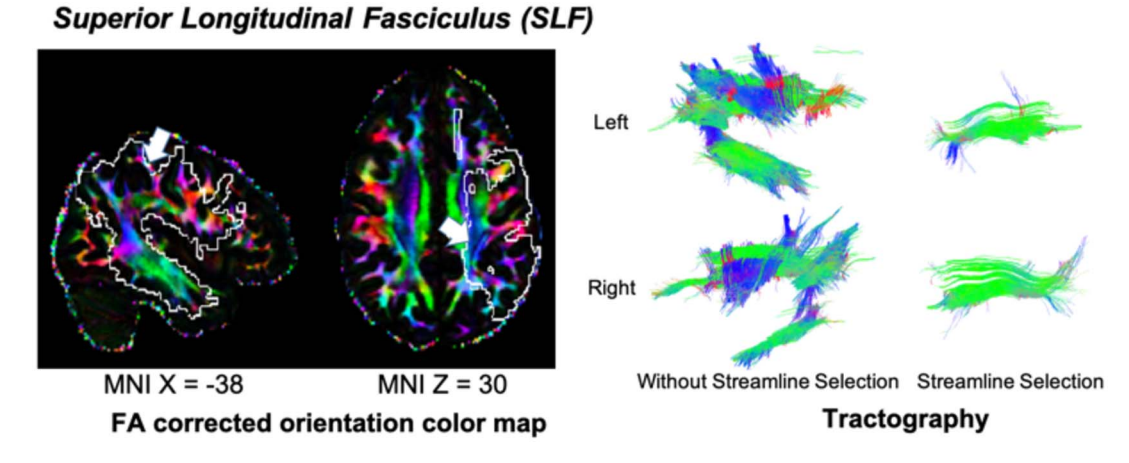


FIG. 8. FA corrected orientation color map of one HCP subject and the tractography of SLF: Left panel—The (probabilistic) SLF mask on the left hemisphere is outlined by white-colored lines with saggital view at MNI X = -38 and axial view at MNI Z = 30. Right panel—SLF tractography before and after streamline selection. (color scheme: green: anterior-posterior; blue: superior-inferior; red: left-right).

voxel and thus is suitable for tracking in crossing fiber regions (Wong et al. (2016)). Moreover, we use the probabilistic masks for the SLF (one on each hemisphere) from the *JHU White-Matter Tractography Atlas* (Hua et al. (2008), Wakana et al. (2007)) as both the seeding mask and the terminating mask. This means that tracking starts from every white-matter voxel within these masks, and the trajectories will be terminated while leaving the SLF region specified by these masks. Another stopping criterion we use is when there is no viable voxel within two steps, where nonviable voxels are those leading to trajectory bending more than 60 degrees or being isotropic (e.g., nonwhite-matter voxels).

Note that the SLF crosses with other fiber tracts, mainly, with the corticospinal tract (CST). As can be seen from the orientation color map of one HCP subject (left panel of Figure 8), the SLF region crosses with the CST (indicated by blue color, as this tract is mainly along the inferior-superior direction). As a result, the reconstructed fibers contain not only those of the SLF but also some of the CST. This can also be seen from the tractography results of one HCP subject (right panel of Figure 8), which shows a big bundle of blue-colored tracks. In order to better dissect the SLF, we further apply *streamline selection*. Here we use binary masks from *AutoPtx* to dissect the SLF from the initial tractography results. Only tracks (streamlines) that pass through both *AutoPtx* binary masks are retained.

The above regional-seeding approach is suitable for extracting a specific pathway (here the SLF) or mapping tracts from a specific region. One advantage of the regional-seeding approach to the whole-brain-seeding approach is that the former is computationally much less intensive and scales better for processing a large number of subjects/images. The regional-seeding approach may also take advantage of any existing knowledge in brain anatomy. A potential disadvantage of the regional-seeding approach is that it may lead to incomplete tract reconstruction. This can be mitigated by using anatomically informed masks, such as those from a white-matter atlas, as we have done here. In Figure S.6 in Hwang et al. (2024), we show the SLF reconstruction results of one HCP subject after streamline selection by the *AutoPtx* masks under different seeding strategies. It shows that our regional-seeding approach does not lose too many fiber tracks, compared to the whole-brain-seeding approach.

4.5. Feature extraction. After tractography and streamline selection, various brain structural connectivity features can be extracted, including the number of streamlines, the length of such streamlines, etc. Here we focus on the difference between the left- and right-hemispheric

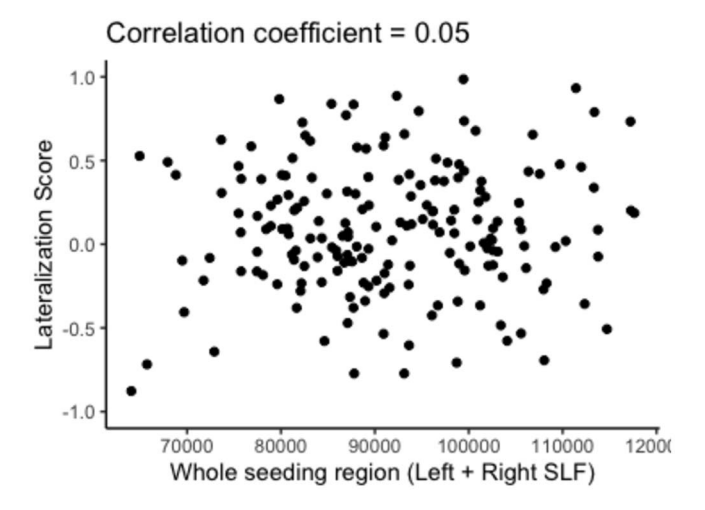


FIG. 9. Lateralization score vs. number of voxels in SLF ROIs: Across 184 sampled HCP subjects.

SLF for the purpose of investigating the lateralization pattern of the SLF and its association with gender and handedness.

Specifically, for each subject we calculate a *lateralization score (LS)* based on the relative difference between the numbers of selected streamlines from the left- and right-hemispheric SLF, respectively,

(11)
$$LS = \frac{\text{Streamlines in Left SLF} - \text{Streamlines in Right SLF}}{(\text{Streamlines in Left SLF} + \text{Streamlines in Right SLF})/2}.$$

Here the denominator serves the purpose of normalization so that the LS from subjects with different brain sizes are comparable. As can be seen from Figure 9, the LS is not correlated with the size of the SLF ROI. A similar score was used by Catani et al. (2007) to quantify lateralization of the language pathway.

4.6. *Group analysis and results*. Reconstructed SLFs of the representative subjects from each gender-handedness group with positive- and negative-lateralization scores are displayed in Figure 10. Moreover, the lateralization score distribution by the gender-handedness group is shown in Figure 11.

We use a *two-way ANOVA* model to study the association between the SLF lateralization score and gender and handedness,

$$Y_{ijk} = \mu + \alpha_i + \beta_j + \gamma_{ij} + \varepsilon_{ijk}, \quad i = 1, 2, j = 1, 2, k = 1, \dots, n_{ij},$$

where Y_{ijk} is the lateralization score, μ is the overall mean, α_i is the main effect of handedness at level i (i=1: left-handed, i=2: right-handed), β_j is the main effect of gender at level j (j=1: female, j=2: male), γ_{ij} is the interaction effect between handedness and gender for the level combination i, j, with constraints $\sum_{i=1}^2 \alpha_i = 0$, $\sum_{j=1}^2 \beta_i = 0$, $\sum_{i=1}^2 \gamma_{ij} = 0$, and ε_{ijk} are i.i.d $N(0, \sigma^2)$ errors. The diagnostic plots (Figure S.8 in Hwang et al. (2024)) show a good model fit.

According to the ANOVA results shown in Table 2, the SLF lateralization is significantly associated with handedness. Moreover, the 95% confidence interval of the contrast between left-handedness and right-handedness is (-0.289, -0.041), which suggests right-handed subjects have a greater left lateralization tendency in the SLF (i.e., larger LS) compared to left-handed subjects. On the other hand, there is no significant gender effect or gender-handedness interaction effect on the SLF lateralization score.

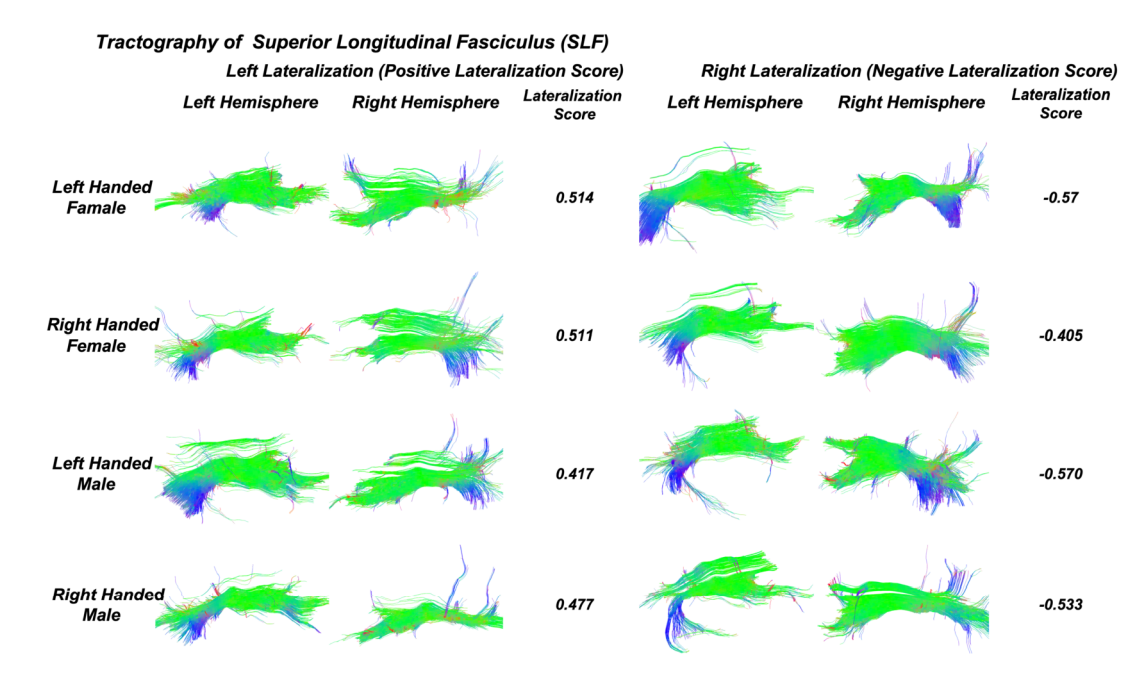


FIG. 10. Reconstructed SLF (sagittal view) of representative HCP subjects. (color scheme: green: anterior-posterior; blue: superior-inferior; red: left-right).

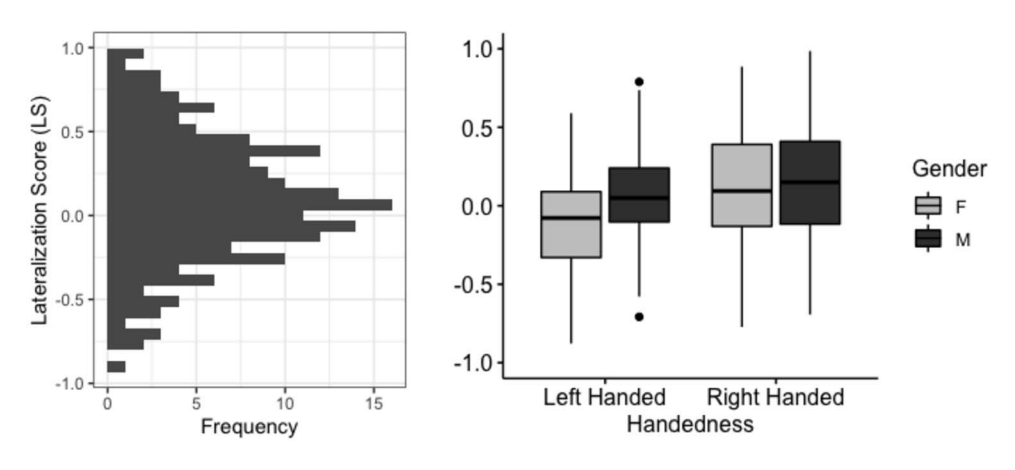


FIG. 11. Lateralization score distribution: Left panel—histogram on all 184 subjects; right panel—box plots by gender-handedness groups.

TABLE 2

HCP D-MRI application: Type III ANOVA results

	d.f.	SS	MS	F-value	p-value
Handedness	1	1.099	1.099	7.911	0.005
Gender	1	0.468	0.468	3.364	0.068
Handedness * Gender	1	0.265	0.265	1.907	0.169
Residuals	180	25.016	0.139		

Note that there are other demographic variables in the HCP data in addition to gender, namely, age and race. The subjects in HCP consist of young adults aged from 22 to 35 and the majority (76%) are White. Height and weight measurements are also available (Figure S.7 in Hwang et al. (2024)). Since we did not expect these variables to have an effect on brain lateralization, we did not include them in the model. Prompted by a reviewer's comment, we also looked into the model including these variables and we reached the same qualitative conclusion, that is, only handedness has a significant effect (Table S.7 in Hwang et al. (2024)).

4.7. Comparison and validation. We also conducted the HCP D-MRI application using DSI Studio (http://dsi-studio.labsolver.org/), a tractography software tool for D-MRI analysis (Yeh et al. (2013), Yeh, Weeden and Tseng (2010)). DSI Studio uses orientation distribution function (ODF) as a local fiber estimation method. ODF is the projection of the diffusion probability density onto the surface of the unit sphere along a ray emanating from a voxel center (Tuch (2002), Tuch (2004)). One limitation of ODF is that it does not preserve the sharp features associated with the underlying fiber bundle orientation. Therefore, if the objective is white matter fiber tract reconstruction, it is expected that the FOD model is more efficient, as it directly models the distribution of fiber orientation within a voxel.

The reconstructed SLF tractography results from our pipeline and *DSI Studio* are visually similar in terms of shape and orientation (Figure S.9 in Hwang et al. (2024)). However, the reconstructed SLF from *DSI Studio* contains a large portion of fiber tracks along the superior-inferior direction (blue-colored tracks), which is likely to be part of the corticospinal tract (CST). As a result, the *DSI Studio* procedure leads to many more selected streamlines than our pipeline. The streamline selection strategy used in our pipeline appears to be more effective in excluding tracks on crossing white-matter fiber tracts (here CST). The extracted features from our pipeline and *DSI Studio* are only weakly positively correlated (Figure S.10 in Hwang et al. (2024)). We suspect that the somewhat low correlation is partially due to differences in preprocessing and masks (on top of using different diffusion MRI models, that is, FOD vs. ODF, as mentioned in the previous paragraph). Lastly, when using the lateralization scores derived from the *DSI Studio* tractography results as responses, there is no significant handedness effect, gender effect, or handedness-gender interaction effect (Table S.8; Figures S.11, S.12 in Hwang et al. (2024)).

For further validation we applied the proposed pipeline and *DSI Studio* to the HCP test-retest data set, which consists of repeated D-MRI measurements for 36 subjects. From Figure S.13 in Hwang et al. (2024), it can be seen that both the proposed pipeline (referred to as *BJS*) and *DSI Studio* are reasonably reproducible with the (Pearson's) correlation coefficients and (Fisher's) intraclass correlation coefficients between the number of streamlines in the left-/right-*SLF* reconstructed from the test data and that from the retest data of the same subject being at least 80%.

As another way for comparison and validation, we also looked into the predictive power of the derived lateralization score in predicting handedness. Specifically, we fitted logistic regression models (using R function glm) with handedness as the response and gender and lateralization score as the predictors and performed 10-fold cross-validation (CV). We calculated the AUC (Area Under the ROC Curve) for each CV fold. While using the lateralization score derived from *BJS*, the average AUC (across 10 CV folds) is 0.666, and the standard deviation is 0.090; While using the lateralization score derived from *DSI-Studio*, the average AUC is 0.624, and the standard deviation is 0.051. Although the predictive power of the SLF lateralization score is not very high, comparatively, the *BJS* derived lateralization score is more powerful than that derived by *DSI-Studio*.

More details can be found in Sections S.3.1 and S.3.2 of the Supplementary Material (Hwang et al. (2024)).

5. Discussion. In this paper we investigate the association between brain structural connectivity and demographic and behavioral features using D-MRI data from the Human Connectome Project. Specifically, we derive a lateralization score for a major association tract, the *superior longitudinal fasciculus (SLF)*, and relate it to gender and handedness. We find significant handedness effects, indicating a difference in the SLF lateralization between left-handed and right-handed individuals. Moreover, we propose a novel computationally efficient method, *BJS*, for estimating the FOD at each brain voxel. We also establish a D-MRI data analysis pipeline that can be utilized for population level associative studies for relating brain anatomic features to external features including demographic, behavioral, or cognitive measurements.

The proposed *BJS* method is scalable for statistical analysis of brain structural connectivity at a population level. It constitutes an effective improvisation of the classical James–Stein shrinkage that solves an ill-conditioned problem with noisy measurements in a nonstandard setting, where an exact diagonalization of the convolution operator in a basis representing the observation vector (D-MRI measurements) is not feasible due to finite sampling effects.

To reconstruct white-matter fiber tracts, the estimated FOD at each voxel needs to provide reasonably accurate fiber orientation information. Based on synthetic experiment results, we believe that the estimated FODs via *BJS* are accurate enough to be used as inputs to a tractography algorithm. Since the orientation of a fiber bundle usually changes smoothly from one voxel to its neighboring voxels, spatial information may be utilized to further improve voxel-level estimation as well tracking results. Some recent works, including Wong et al. (2016) and Rao et al. (2016), have been proposed for fiber reconstruction where spatial constraint is incorporated. It is conceivable that the *BJS* estimator may be further improved if neighboring voxel information is utilized. We leave this as a future research direction.

We also validated the *BJS* pipeline, using the HCP test-retest data set, and found the reconstruction results (in terms of the number of streamlines) reproducible with correlation coefficients between results from the test data and retest data around 90%. There are other software packages or pipelines available for D-MRI data analysis, including *FSL* (Jenkinson et al. (2012)) and *PSC* (Zhang et al. (2018)). Although both may potentially be used for the type of applications presented in this paper, we did not compare with *FSL*, due to its slowness in tractography, and we did not compare with *PSC*, as we could only locate a github repository instead of a packaged software. Nevertheless, a more comprehensive comparison with existing D-MRI data processing and analysis tools would further reveal applicability and limitations of *BJS*. This will be a future research direction.

Although a large proportion of the neuronal fiber bundles can be explained by the reconstructed neuronal fiber tracks based on D-MRI, it is not sufficient to represent the actual fiber system in the brain. Also, the estimated fiber composition can be different depending on the tractography algorithm (Jones, Knösche and Turner (2013)). Despite these challenges, this paper successfully demonstrates that it is possible to extract meaningful structural connectivity information from reconstructed neuronal fiber tracts, based on D-MRI data, and to relate such information with external features.

Acknowledgments. The authors would like to thank Hao Yan, Jilei Yang, and Raymond Wong for sharing codes for peak detection, fiber tracking, and generating synthetic D-MRI data. Data used in the real application were provided by the Human Connectome Project, WU-Minn Consortium (Principal Investigators: David Van Essen and Kamil Ugurbil; 1U54MH091657) funded by the 16 NIH Institutes and Centers that support the NIH Blueprint for Neuroscience Research and by the McDonnell Center for Systems Neuroscience at Washington University.

Seungyong Hwang is also affiliated with Department of Genetics, Stanford University.

Funding. This research is supported by the following grants: NSF DMS-1713120 (D.P.), DMS-1811405(T.L., D.P.), DMS-1811661(T.L.), DMS-1915894(S.H., D.P., J.P.), DMS-1916125 (S.H., T.L.), and NIH 1R01EB021707(D.P., J.P.).

SUPPLEMENTARY MATERIAL

Supplementary text (DOI: 10.1214/23-AOAS1781SUPPA; .pdf). A supplementary text with additional details on FOD estimators, synthetic experiments results and the HCP D-MRI application.

Codebase (DOI: 10.1214/23-AOAS1781SUPPB; .zip). Codes and example scripts for synthetic experiments and the HCP application can also be found at https://github.com/vic-dragon/BJS, together with a detailed manual on D-MRI batch downloading and preprocessing.

REFERENCES

- ALEXANDER, A. L. (2010). Deterministic white matter tractography. In *Diffusion MRI: Theory, Methods, and Applications* (D. K. Jones, ed.) 201–213. Oxford Univ. Press, London.
- AMEMIYA, K., NAITO, E. and TAKEMURA, H. (2021). Age dependency and lateralization in the three branches of the human superior longitudinal fasciculus. *Cortex* **139** 116–133.
- BASSER, P. J., PAJEVIC, S., PIERPAOLI, C., DUDA, J. and ALDROUBI, A. (2000). In vivo fiber tractography using DT-MRI data. *Magn. Reson. Med.* **44** 625–632. https://doi.org/10.1002/1522-2594(200010)44:4<625:: aid-mrm17>3.0.co:2-o
- BUDISAVLJEVIC, S., CASTIELLO, U. and BEGLIOMINI, C. (2021). Handedness and white matter networks. Neuroscientist 27 88–103. https://doi.org/10.1177/1073858420937657
- BUDISAVLJEVIC, S., DELL'ACQUA, F., ZANATTO, D., BEGLIOMINI, C., MIOTTO, D., MOTTA, R. and CASTIELLO, U. (2017). Asymmetry and structure of the fronto-parietal networks underlie visuomotor processing in humans. *Cereb. Cortex* 27 1532–1544. https://doi.org/10.1093/cercor/bhv348
- CAI, T. T. (1999). Adaptive wavelet estimation: A block thresholding and oracle inequality approach. *Ann. Statist.* **27** 898–924. MR1724035 https://doi.org/10.1214/aos/1018031262
- CAI, T. T., LOW, M. G. and ZHAO, L. H. (2009). Sharp adaptive estimation by a blockwise method. J. Non-parametr. Stat. 21 839–850. MR2572586 https://doi.org/10.1080/10485250903142663
- CARMICHAEL, O., CHEN, J., PAUL, D. and PENG, J. (2013). Diffusion tensor smoothing through weighted Karcher means. *Electron. J. Stat.* 7 1913–1956. MR3084676 https://doi.org/10.1214/13-EJS825
- CATANI, M. (2010). The functional anatomy of white matter: From postmortem dissections to in vivo virtual tractography. In *Diffusion MRI: Theory*, *Methods*, *and Applications* (D. K. Jones, ed.) 5–18. Oxford Univ. Press, London.
- CATANI, M., ALLIN, M. P. G., HUSAIN, M., PUGLIESE, L., MESULAM, M. M., MURRAY, R. M. and JONES, D. K. (2007). Symmetries in human brain language pathways correlate with verbal recall. *Proc. Natl. Acad. Sci. USA* **104** 17163–17168.
- CAVALIER, L. and TSYBAKOV, A. (2002). Sharp adaptation for inverse problems with random noise. *Probab. Theory Related Fields* **123** 323–354. MR1918537 https://doi.org/10.1007/s004400100169
- CAVALIER, L. and TSYBAKOV, A. B. (2001). Penalized blockwise Stein's method, monotone oracles and sharp adaptive estimation *Math. Methods Statist.* **10** 247–282. MR1867161
- DE GROOT, M., VERNOOIJ, M. W., KLEIN, S., IKRAM, M. A., VOS, F. M., SMITH, S. M., NIESSEN, W. J. and ANDERSSON, J. L. R. (2013). Improving alignment in tract-based spatial statistics: Evaluation and optimization of image registration. *NeuroImage* **76** 400–411.
- DESCOTEAUX, M., ANGELINO, E., FITZGIBBONS, S. and DERICHE, R. (2006). Apparent diffusion coefficients from high angular resolution diffusion imaging: Estimation and applications. *Magn. Reson. Med.* **56** 395–410.
- DESCOTEAUX, M., ANGELINO, E., FITZGIBBONS, S. and DERICHE, R. (2007). Regularized, fast and robust analytical Q-ball imaging. *Magn. Reson. Med.* **58** 497–510.
- ESSEN, D. C. V., SMITH, S. M., BARCH, D. M., BEHRENS, T. E. J., YACOUB, E. and UGURBIL, K. (2013). The Wu-Minn human connectome project: An overview. *NeuroImage* **80** 62–79.
- GHARABAGHI, A., KUNATH, F., ERB, M., SAUR, R., HECKL, S., TATAGIBA, M., GRODD, W. and KARNATH, H.-O. (2009). Perisylvian white matter connectivity in the human right hemisphere. *BMC Neurosci.* **10** 15. https://doi.org/10.1186/1471-2202-10-15

- GLASSER, M. F., SOTIROPOULOS, S. N., WILSON, J. A., COALSON, T. S., FISCHL, B., ANDERSSON, J. L., XU, J., JBABDI, S., WEBSTER, M. et al. (2013). The minimal preprocessing pipelines for the human connectome project. *NeuroImage* 80 105–124.
- GOLDENSHLUGER, A. and TSYBAKOV, A. (2001). Adaptive prediction and estimation in linear regression with infinitely many parameters. *Ann. Statist.* **29** 1601–1619. MR1891740 https://doi.org/10.1214/aos/1015345956
- GUDBJARTSSON, H. and PATZ, S. (1995). The Rician distribution of noisy MRI data. *Magn. Reson. Med.* 34 910–914. https://doi.org/10.1002/mrm.1910340618
- HEALY, D. M. JR., HENDRIKS, H. and KIM, P. T. (1998). Spherical deconvolution. J. Multivariate Anal. 67 1–22. MR1659108 https://doi.org/10.1006/jmva.1998.1757
- HOSEY, T., WILLIAMS, G. and ANSORGE, R. (2005). Inference of multiple fiber orientations in high angular resolution diffusion imaging. *Magn. Reson. Med.* 54 1480–1489.
- HOUSTON, J., ALLENDORFER, J., NENERT, R., GOODMAN, A. M. and SZAFLARSKI, J. P. (2019). White matter language pathways and language performance in healthy adults across ages. *Front. Neurosci.* **13** 1185. https://doi.org/10.3389/fnins.2019.01185
- HOWELLS, H., THIEBAUT DE SCHOTTEN, M., DELL'ACQUA, F., BEYH, A., ZAPPALÀ, G., LESLIE, A., SIMMONS, A., MURPHY, D. G. and CATANI, M. (2018). Frontoparietal tracts linked to lateralized hand preference and manual specialization. *Cereb. Cortex* 28 2482–2494.
- HUA, K., ZHANG, J., WAKANA, S., JIANG, H., LI, X., REICH, D. S., CALABRESI, P. A., PEKAR, J. J., VAN ZIJL, P. C. M. et al. (2008). Tract probability maps in stereotaxic spaces: Analyses of white matter anatomy and tract-specific quantification. *NeuroImage* 39 336–347.
- HWANG, S., LEE, T. C. M., PAUL, D. and PENG, J. (2024). Supplement to "Estimating Fiber Orientation Distribution with Application to Study Brain Lateralization using HCP D-MRI Data." https://doi.org/10.1214/23-AOAS1781SUPPA, https://doi.org/10.1214/23-AOAS1781SUPPB
- JENKINSON, M., BANNISTER, P., BRADY, M. and SMITH, S. (2002). Improved optimization for the robust and accurate linear registration and motion correction of brain images. *NeuroImage* 17 825–841. https://doi.org/10. 1016/s1053-8119(02)91132-8
- JENKINSON, M., BECKMANN, C. F., BEHRENS, T. E. J., WOOLRICH, M. W. and SMITH, S. M. (2012). FSL. *NeuroImage* **62** 782–790. https://doi.org/10.1016/j.neuroimage.2011.09.015
- JONES, D. K. (2010). Diffusion MRI: Theory, Methods, and Applications. Oxford Univ. Press, London.
- JONES, D. K., KNÖSCHE, T. R. and TURNER, R. (2013). White matter integrity, fiber count, and other fallacies: The do's and don'ts of diffusion MRI. *NeuroImage* 73 239–254. https://doi.org/10.1016/j.neuroimage.2012. 06.081
- LAURENT, B. and MASSART, P. (2000). Adaptive estimation of a quadratic functional by model selection. *Ann. Statist.* **28** 1302–1338. MR1805785 https://doi.org/10.1214/aos/1015957395
- LE BIHAN, D., MANGIN, J. F., POUPON, C., CLARK, A. C., PAPPATA, S., MOLKO, N. and CHABRIAT, H. (2001). Diffusion tensor imaging: Concepts and applications. *J. Magn. Reson. Imaging* 13 534–546.
- LÓPEZ-VICENTE, M., LAMBALLAIS, S., LOUWEN, S., HILLEGERS, M., TIEMEIER, H., MUETZEL, R. L. and WHITE, T. (2021). White matter microstructure correlates of age, sex, handedness and motor ability in a population-based sample of 3031 school-age children. *NeuroImage* 227 117643.
- MAKRIS, N., KENNEDY, D. N., McINERNEY, S., SORENSEN, A. G., WANG, R., CAVINESS JR, V. S. and PANDYA, D. N. (2004). Segmentation of subcomponents within the superior longitudinal fascicle in humans: A quantitative, in vivo, DT-MRI study. *Cereb. Cortex* **15** 854–869.
- MCCARTHY, P. (2020). FSLeyes 0.34.0. Available at https://doi.org/10.5281/zenodo.3937147.
- MORI, S. (2007). Introduction to Diffusion Tensor Imaging. Elsevier, Amsterdam.
- MUSCHELLI, J. (2018). neurohcp: Human 'Connectome' Project Interface. R package version 0.8.1.
- MUSCHELLI, J., SWEENEY, E., LINDQUIST, M. and CRAINICEANU, C. (2015). fslr: Connecting the FSL software with R. R J. 7 163–175.
- NIMSKY, C., GANSLANDT, O. and FAHLBUSCH, R. (2006). Implementation of fiber tract navigation. *Neurosurgery* **58** 292–303.
- RAO, S., IBRAHIM, J. G., CHENG, J., YAP, P.-T. and ZHU, H. (2016). SR-HARDI: Spatially regularizing high angular resolution diffusion imaging. *J. Comput. Graph. Statist.* **25** 1195–1211. MR3572036 https://doi.org/10.1080/10618600.2015.1105750
- SCHWARZ, G. (1978). Estimating the dimension of a model. Ann. Statist. 6 461-464. MR0468014
- SEIZEUR, R., MAGRO, E., PRIMA, S., WIEST-DAESSLÉ, N., MAUMET, C. and MORANDI, X. (2014). Corticospinal tract asymmetry and handedness in right- and left-handers by diffusion tensor tractography. *Surg. Radiol. Anat.* **36** 111–124. https://doi.org/10.1007/s00276-013-1156-7
- SMITH, S. M., JENKINSON, M., JOHANSEN-BERG, H., RUECKERT, D., NICHOLS, T. E., MACKAY, C. E., WATKINS, K. E., CICCARELLI, O., CADER, M. Z. et al. (2006). Tract-based spatial statistics: Voxelwise analysis of multi-subject diffusion data. *NeuroImage* 31 1487–1505. https://doi.org/10.1016/j.neuroimage.2006.02.024

- SPORNS, O. (2011). Networks of the Brain. MIT Press, Cambridge.
- SZAFLARSKI, J. P., RAJAGOPAL, A., ALTAYE, M., BYARS, A. W., JACOLA, L. and SCHMITHORST, V. (2012). Left-handedness and language lateralization in children. *Brain Res.* **1433** 85–97.
- TOURNIER, J., CALAMANTE, F. and CONNELLY, A. (2007). Robust determination of the fibre orientation distribution in diffusion MRI: Non-negativity constrained super-resolved spherical deconvolution. *NeuroImage* **35** 1459–1472. https://doi.org/10.1016/j.neuroimage.2007.02.016
- TOURNIER, J., CALAMANTE, F., GADIAN, D. G. and CONNELLY, A. (2004). Direct estimation of the fiber orientation density function from diffusion-weighted MRI data using spherical deconvolution. *NeuroImage* **23** 1176–1185. https://doi.org/10.1016/j.neuroimage.2004.07.037
- Tuch, D. S. (2002). Diffusion MRI of complex tissue structure Ph.D. thesis Massachusetts Institute of Technology.
- TUCH, D. S. (2004). Q-ball imaging. Magn. Reson. Med. 52 1358–1372.
- Tuch, D. S., Reese, T. G., Wiegell, M. R., Makris, N., Belliveau, J. W. and Wedeen, V. J. (2002). High angular resolution diffusion imaging reveals intravoxel white matter fiber heterogeneity. *Magn. Reson. Med.* **48** 577–582. https://doi.org/10.1002/mrm.10268
- WAKANA, S., CAPRIHAN, A., PANZENBOECK, M. M., FALLON, J. H., PERRY, M., GOLLUB, R. L., HUA, K., ZHANG, J., JIANG, H. et al. (2007). Reproducibility of quantitative tractography methods applied to cerebral white matter. *NeuroImage* **36** 630–644.
- WONG, R. K. W., LEE, T. C. M., PAUL, D., PENG, J. and INITIATIVE, A. D. N. (2016). Fiber direction estimation, smoothing and tracking in diffusion MRI. Ann. Appl. Stat. 10 1137–1156. MR3553216 https://doi.org/10.1214/15-AOAS880
- WOOLRICH, M. W., JBABDI, S., PATENAUDE, B., CHAPPELL, M., MAKNI, S., BEHRENS, T., BECKMANN, C., JENKINSON, M. and SMITH, S. M. (2009). Bayesian analysis of neuroimaging data in FSL. *NeuroImage* 45 S173–S186.
- YAN, H., CARMICHAEL, O., PAUL, D., PENG, J. and ADNI (2018). Estimating fiber orientation distribution from diffusion MRI with spherical needlets. *Med. Image Anal.* 46 57–72.
- YEH, F.-C., VERSTYNEN, T. D., WANG, Y., FERNÁNDEZ-MIRANDA, J. C. and TSENG, W.-Y. I. (2013). Deterministic diffusion fiber tracking improved by quantitative anisotropy. *PLoS ONE* 8.
- YEH, F. C., WEEDEN, V. J. and TSENG, W. Y. I. (2010). Generalized q-sampling imaging. *IEEE Trans. Med. Imag.* 29 1626–1635.
- ZHANG, Y., BRADY, M. and SMITH, S. (2001). Segmentation of brain MR images through a hidden Markov random field model and the expectation-maximization algorithm. *IEEE Trans. Med. Imag.* **20** 45–57. https://doi.org/10.1109/42.906424
- ZHANG, Z., DESCOTEAUX, M., ZHANG, J., GIRARD, G., CHAMBERLAND, M., DUNSON, D., SRIVASTAVA, A. and ZHU, H. (2018). Mapping population-based structural connectomes. *NeuroImage* **172** 130–145.